Analytical and Bioanalytical Chemistry
October 2008, Volume 392 (3) : Pages 551-560
http://dx.doi.org/10.1007/s00216-008-2273-8

Understanding otolith biomineralization processes: new insights into microscale spatial distribution of organic and mineral fractions from Raman microspectrometry

Aurélie Jolivet[1, *], Jean-François Bardeau[2], Ronan Fablet[1, 3], Yves-Marie Paulet[4], Hélène de Pontual[1]

[1] Ifremer, Laboratoire de Sclérochronologie des Animaux Aquatique STH/LASAA, Z.I. Pointe du diable, BP 70, 29280 Plouzané, France
[2] Laboratoire de Physique de l'Etat Condensé, Faculté des Sciences, Université du Maine, Avenue Olivier Messiaen, 72085 Le Mans Cedex 09, France
[3] Institut Telecom/ Telecom Bretagne, LabSTICC, Technopole Brest Iroise, CS83818, 29238 Brest Cedex 03, France
[4] LEMAR, UMR 6539 CNRS, Institut Universitaire Européen de la Mer, Place Nicolas Copernic, 29 280 Plouzané, France

*: Corresponding author : A. Jolivet, email address : Aurelie.Jolivet@ifremer.fr

Abstract:

It is generally accepted that the formation of otolith microstructures (L- and D-zones) and in particular the organic and mineral fractions vary on a daily basis. Raman microspectrometry provides a nondestructive technique that can be used to provide structural information on organic and mineral compounds. We applied it to thin otolith sections of hake in order to address the following issues: (1) the simultaneous characterization of variations in the organic and mineral fractions both in the core area and along successive otolith microstructures; (2) elucidation of significant differences between these fractions; (3) quantification of the effects of etching and staining protocols on otolith structures. The primordium appeared as a punctual area depicting higher luminescence and greater concentrations in organic compounds containing CH groups. Sulcus side showed similar composition suggesting that the contact of the otolith with the macula and its orientation in otosac occur rapidly (about 10 days). The characterization of L- and D-zones in the opaque zones indicated that both structures contained organic and aragonitic fractions with cyclic and synchronous variations. Contrary to the results obtained after EDTA etching, L-zones depicted greater concentrations in organic compounds containing CH groups, whereas D-zones appear richer in aragonite. This organic fraction seemed to be revealed by Mutvei's staining and was affected by EDTA etching which suggests that it corresponds to the soluble fraction of organic matrix. Such results indicate that L- and D-zones differ in their respective organic constituents. Raman microspectrometry thus appears as a powerful technique to acquire quantitative information that is required for a better understanding of otolith biomineralization.

Keywords: Core - L- and D-zones - Aragonite - Staining - Acid etching

Introduction

Otoliths are calcareous concretions in fish inner ears. Their accretional growth follows a circadian rhythm that is physiologically controlled and influenced by environmental conditions [1, 2]. The formation of daily L- and D-zones result, also referred to as microstructures as well as of opaque and translucent macrostructures (Figure 1). The otoliths act as biological archives providing the basis for the reconstruction of individual life traits and environmental parameters. They thus deliver invaluable information in fisheries sciences and marine ecology [3]. However in many cases the interpretation schemes of both structural and chemical information remain incomplete and debatable. New advances in the analysis and the understanding of otolith biomineralization, especially regarding the relationships between the physico-chemical characteristics of the accretion and the associated environmental and physiological conditions, are of key importance to fully exploit the potential of these biological archives [3, 4].

Overall the calcium carbonate fraction, mainly in aragonite form, represents 90-99 % of the total mass of fish otoliths. The remaining 1-10% includes the organic matrix, composed of collagens, proteoglycans and proteins [5-7]. The role of organic matrix in the formation of the deposited layer is not fully understood, although different studies have demonstrated that it controls the biomineralization of the otolith [7, 8]. L- and D-zones have been described as depicting different compositions in term of organic and mineral fractions [9-11] by global quantitative and fine scale qualitative experiments. To our knowledge, these compositions have never been quantified at a micro-scale. Given the spatial resolution and the capacity of simultaneously characterizing organic and mineral compounds, Raman micro-spectrometry is particularly well-suited to address these issues.

Raman micro-spectrometry is a non destructive technique which provides a quantitative characterization of vibrational physico-chemico features of both organic and

mineral compounds. Regarding calcified structures, Raman micro-spectrometry permits discriminating vaterite, aragonite and calcite in otoliths of different species [12-15], and is also particularly well-suited to study the organic matrix of corals [16], the degradation of skeletal organic matrix [17] and mollusc shell pigments [18]. More recently Raman micro-spectrometry was used to identify and analyze variations of the characteristics of the organic matrix in fish otoliths [19].

Here, we use Raman micro-spectrometry to investigate physico-chemical variations in the organic and mineral constituents of fish otoliths in relation to observed micro-structures. Experiments are reported for thin sections of European hake (*Merluccius merluccius*) otoliths. Our main contributions are three-fold: 1) characterizing mineral and organic fractions within otoliths microstructures (namely, primordium and L- and D-zones); 2) elucidating significant differences between L- and D- zones; 3) highlighting the differential effects of etching and staining on the organic and mineral fractions of these zones.

[Figure 1 about here]

Material and Methods

Otolith samples

We considered a series of otoliths extracted from hake caught in the Bay of Biscay in June 2005 and 2007 or reared in controlled facilities (Table 1). Larval, juvenile and adult fish were available and fish size (total length) ranged from 4.3 mm (larva size) to 50 cm. To obtain thin sections, the standard otolith preparation method consisted of: 1) embedding in epoxy resin, 2) sectioning in transverse or sagittal plane, 3) grinding, and 4) polishing to the core. Larval otolith was extracted under polarized light, mounted on an epoxy resin drop and directly analysed on sagittal plan without any further preparation.

[Table 1 about here]

Etching and staining protocols

Etching was performed using a 5% EDTA (ethylene diamine tetra-acetate) solution at pH 7. EDTA is as calcium chelator frequently used for otolith decalcification. Section S7 was exposed to the EDTA solution for a period of 90 seconds after which the sample was rinsed with milliQ water.

To enhance the optical contrast of otolith structures, otolith sections were stained. For this purpose, we used Mutvei's solution [20] composed in the following manner: 500 ml 1% acetic acid for 500 ml 25% glutaraldehyde and ca. 5 to 10 g alcian blue. The latter stains mucopolyssacharides and glycosaminoglycans. This dye also performs a slight etching of the surface as it contains diluted acetic acid. Section S8 was immersed in the Mutvei's solution for 10 min at 45°C and subsequently rinsed with milliQ water.

Analyses of fine-scale otolith structures

Three different types of analysis were carried out at core area, micro-increments in L- and D-zones on 1) standard preparations, 2) EDTA etched preparations, and 3) preparations stained with Mutvei's solution. Details about the analysis are summarized in Table 1.

For the core area, three transversal sections (S1-S3) were analysed. In addition, the sagittal section of an 18 days larva otolith (S4) was considered. Dorso-ventral Raman transects spectra centred on the primordium were acquired with steps varying from 2.5 to 6 µm. For S4, the transect was 14 µm long with points at 7, 12 and 14 µm. In addition, a 2D mapping centred on the primordium was acquired on S3.

Regarding the characterization of L- and D-zones, Raman spectra on transects covering several successive increments were acquired in opaque zones of two sagittal otolith sections (S5 and S6). The sagittal plane was preferred to the transverse one as wider D- and L-zones, typically 2 and 4 µm respectively, were observed.

Regarding EDTA etching, Raman spectra were acquired before and after etching on the opaque zone of S7 along a transect covering two D-zones and two L-zones. Raman measurements were carried out after staining within an opaque zone of S8 along a transect covering three D-zones and two L-zones.

Raman spectrometry

A micro-Raman spectrometer (Jobin-Yvon T64000) equipped with a confocal system and a motorized microscope stage (for Raman mapping purpose) was used and specific experimental conditions were defined. A coherent spectrum argon/krypton ion laser was used to produce radiation with a wavelength of 514.5 nm and a good signal-noise ratio. The laser was focused onto the sample by using a microscope equipped with a x100 objective. The resulting spatial resolution is about 1-2 µm. The scattered light was analysed by a spectrometer with a single monochromator (600 gratings mm^{-1}), coupled to a nitrogen cooled CCD detector. To check that the experimental setting is non-destructive for fish otoliths, several Raman spectra were recorded at the same points between 20 to 200 mW. No heating alteration was observed on spectra when controlling relative intensities and profiles. For the analysis of the otolith core and microstructures, a 50 mW laser power was selected. Stained otoliths were analysed with a 10 mW laser. Spectra were accumulated two to four times with exposure times varying from 30 to 300 s depending on the sample. The depth of analysis was systematically set to 2 µm below the surface to avoid possible contamination linked to surface preparations.

142

143 **Analysis of Raman spectra**

144 Raman spectra were corrected for background luminescence using baseline subtraction. In the
145 subsequent analysis, reported Raman spectra are baseline corrected and normalized with
146 respect to a reference acquisition time of 50 s and a reference of 50 mW laser. The positions
147 and integrated intensities of identifiable vibrational bands on spectra were determined using
148 the LABSPEC software. Optical images under transmitted light were acquired before each
149 analysis to record the locations of Raman analysis for subsequent treatment.

150

151 **Quantitative analysis for characterization of aragonitic and organic fractions**

152 With respect to Raman spectra of fish otoliths, 14 vibrational bands can be directly attributed
153 to aragonite [21]: symmetric stretching mode (1085 cm^{-1}), anti-symmetric stretching modes
154 (1462, 1574 cm^{-1}), in plane bending modes of CO_3^{2-} (701 and 705 cm^{-1}) and the lattice modes
155 (9 peaks between 113 and 284 cm^{-1}) (Figure 2A). The broad bands observed at 2950-3070 and
156 3390 cm^{-1} are respectively associated to CH and OH stretching modes (Figure 2B). The
157 aragonite peak at 1085 cm^{-1} was chosen as the reference peak for the spectra normalization. In
158 this study, we considered the ratio between the response of the CH-group and the peak of
159 aragonite at 1085 cm^{-1} as a proxy of the ratio between the organic and mineral fraction of the
160 otolith structures.

161

162 [Figure 2 about here]

163

164 Figure 3 shows the Raman spectra of Mutvei's solution and of the stained otolith. The
165 Mutvei's solution is known to result in a specific response between 1200 and 1700 cm^{-1}. From
166 the Raman analysis of the stained otolith section, we determined the relative fraction of the

stained organic matrix *vs* the aragonitic fraction. As the aragonitic peak at 1085 cm^{-1} is occluded by the Raman response of the dye, we used the peaks between 100 and 300 cm^{-1} as the aragonitic references. The ratio between this aragonitic reference and the dye-specific Raman response between 1200 and 1700 cm^{-1} was then calculated.

[Figure 3 about here]

Glossary

For the sake of clarity, we abbreviated organic matrix (OM), Aragonite (AR) represented by the band at 1085 cm^{-1}, CH-group (CH) the whole bands observed in the region 2950-3070 cm^{-1}, OH-group (OH) bands in the region 3390-4000 cm^{-1}, and OM/AR, CH/AR and OH/AR, the respective ratios between the integrated intensity of the bands described previously.

Results

Core area

For samples S1-S4, the main peaks of the Raman spectra acquired in the core area are reported in Table 2. Their wavelength and possible assignments to known vibrational modes are given and compared to previous results [19, 22-24].

[Table 2 about here]

Figure 4 shows Raman spectra of the S1 primordium zone. A greater luminance was observed in conjunction with the primordium than the surrounding points. The intensities of amides and amino acids peaks reached maxima in the primordium (Figure 4B) as well as CH and OH groups (Figure 5A). Similar results were observed for S2-S4 samples as shown in Figure 5B with the evolution of CH/AR as a function of the distance from the primordium.

The primordium was also shown to be 10 times more concentrated in CH than points located at 18 µm in the dorsal and ventral directions. Besides, the spatial distribution of the CH/AR ratio in the core area (30 µm x 40 µm mapping around the primordium) of S3 is reported (Figure 6). Whereas the decrease of the CH/AR ratio along the anti-sulcus, dorsal and ventral directions is isotropic and similar to the profile depicted in Figure 5, the sulcus area is characterized by a greater CH/AR ratio.

[Figure 4-6 about here]

L- and D-zones

Analyses of L- and D-zones were carried out on S5 and S6. The Raman spectra of one L-zone and one D-zone are shown in Figure 7 along with the evolution of the AR, CH (Figure 8B) and CH/AR ratio (Figure 8C) along the transects considered. OH-response was relatively stable compared to the CH-signature, which varies according to alternating L- and D-zones (Figure 7). Both CH and AR responses showed cyclic variations but different ranges of variations (Figure 8B). Cycles with maxima located on L-zones and minima on D-zones were also observed for CH/AR (Figure 8C). L-zones display a greater relative concentration in CH and D-zones a greater relative concentration of AR (Figure 8B). Similar results were obtained from the analysis of the second S6 sample.

[Figure 7-8 about here]

Effects of EDTA etching

The variation of CH/AR along the considered transects before and after etching is shown in Figure 9. Whereas CH/AR depicted a maximum response in L-zones before etching, the

maxima were located in D-zones after etching. AR responses after etching were lowered by a factor of 0.8. On the contrary, CH variations were greater by a factor of 1.3 after etching. This resulted in a greater CH/AR after etching (Figure 9).

[Figure 9 about here]

Effects of staining

The analyses of the Raman responses of the AR fraction and of the dye after otolith staining with Mutvei's solution are reported in Figure 10 for a transverse otolith section. Optically L-zones displayed greater degree of staining. The Raman response of the Mutvei's dye on otolith showed cyclic variations in phase with the variations in AR. Maxima are located in L-zones (Figure 10A), and the ratio between these two signatures varied according to cyclic behaviour with maxima in L-zones (Figure 10B).

[Figure 10 about here]

Discussion

Core

The analysis of the Raman spectra confirmed that primordium is a very specific point of the otolith with a greater concentration of CH and other organic compounds, such as collagen and amino acids, compared to other areas of the otolith. SEM observations lead to similar conclusions with the primordium being detected as a point of greater density [25]. According to Pisam *et al.* [26] this structure is highly concentrated in glycogen and collagens. The analysis of the Raman spectra also showed that this feature was very punctual, corresponding to the primordium (about 2µm width). Zhang *et al.* [19] recently reported a qualitative Raman

characterization of small yellow croaker and discussed the identification of main organic compounds namely collagen with signatures of amides I, III, IV and V and aromatic amino acid such as phenylalanine, tyrosine and tryptophan. It is worth noting that Zhang *et al.* [19] did not show and discuss the 1050-1200 cm^{-1}spectral region. For this reason, no comparison can be made in this frequency range. Otherwise, most of the peaks found in our study have been observed by Zhang *et al.* [19] except Phe-signatures at 1003 and 1031 cm^{-1} and Trp-peak at 1555 cm^{-1} that might be masked by the strong aragonite signatures at 1085 and 1574 cm^{-1} respectively. The peak observed at 1272 cm^{-1} in our spectra was integrated in a larger band (1206 and 1280 cm^{-1}) with maximum at 1234 cm^{-1}. In contrary, some peaks observed for samples S1-S3 that were mentioned by Zhang *et al.* [19]. These peaks correspond to Tyr-signatures at 1185 and 1610 cm^{-1}, CN group at 1110 cm^{-1} and CH-stretch at 3067 cm^{-1}.

The 2D mapping of the region surrounding the primordium exhibited interesting features. The concentration of the CH-related compounds was found to decrease from the primordium zone along the dorsal, ventral and anti-sulcus directions. Regarding the sulcus area, a similar initial decrease was observed up to 9µm from the primordium. Subsequently, the concentration of the CH-related compounds increased again, up to values comparable to those of the primordium zone. It is known that the sulcus zone is in contact with the macula [27-29]. Moreover, the cells of the macula and of the adjacent zone are the sources of both organic precursors and calcium ions in the endolymph [30]. Given the distance from the primordium to the valley is about 9 µm, this observation suggests that the otolith was in close proximity to the macula at a recent stage and thus oriented in the otosac. Such link would be established at about 10 days post hatching [31].

L and D-zones

Previous studies on the characterization of L- and D-zones concluded that D-zones were richer in OM than L-zones [25, 32]. Such characterizations of L- and D-zones were carried out after EDTA etching. Under this condition, the reported Raman characterizations provided similar results. Variations of AR responses depicted maxima located on L-zones, and conversely for CH, such that the relative proportion of CH *vs* AR was greater in the D-zones than in L-zones after etching.

The analysis of the Raman spectra on L- and D-zones before EDTA etching led to different conclusions. The responses of the organic compounds and aragonitic fraction as well as the CH/AR were greater on L-zones than on D-zones. As a consequence, these results contradict the widely accepted model stating that organic material concentration is greater in D-zones [1]. Whereas differences in crystal organization (e.g., crystal orientation and density) might affect the absolute values of the responses of the aragonite and organic compounds, such physical properties should not affect the CH/AR. L-zones are richer in CH-related organic fraction (relatively to the AR fraction) which suggests that L- and D-zones are associated with different biomineralization processes. Both of these processes involve the biomineralization of organic and mineral factions but some organic compounds being more specific to L-zones.

The comparison of the results before and after etching pointed out that the action of EDTA etching reversed the analysis of the CH/AR in L- and D-zones. It is shown that EDTA etching acted differently on L- and D-zones. Hence, L- and D-zones did not only differ in the relative proportions of organic and mineral compounds but also in their structural organization, such that D-zones are less sensitive to EDTA etching. D-zones appeared to be richer in CH after etching. That could be explained by highlighted CH signature after AR etching. As suggested by SEM observations of thin otolith sections [25, 32] D-zones may be associated with a denser organic mesh, which CH organic compounds would weakly

participate to, such that the overall deposited structure would be more stable in D-zones. This inversion presupposed that L- and D-zones contained different OM compositions with L-zones richer in compounds that are soluble in EDTA.

Mutvei's staining reveals etch-resistant lines called growth lines and etched depressions called growth increments [20]. Alcian blue in Mutvei's solution is used as an indicator of acid mucopolyssacharides [33] and underlined carbon and nitrogen content of carbohydrates [34]. These compounds have been detected in the soluble organic matrix extracted from several fish species (*Salmo salar* [35]; *Oncorhynchus mykiss* and *Psetta maxima* [36] and *Gadus morhua* [37]). L-zones were optically blue-stained by the dye and the agent signature followed that of AR. These results corroborated the above conclusion stating that L-zones are richer in organic compounds revealed by the dye, such as polysaccharides (carbohydrates such as glycogen). Mutvei's staining was also shown to react more strongly with organic compounds soluble in EDTA [20]. Therefore, the agreement between Raman characterization of CH responses and Mutvei's staining in L-zones may suggest that CH-responses are partly associated with the EDTA-soluble fraction of the OM. In Murayama *et al.* [6], the OMP-1, a collagen-like protein assumed to be involved in structuring the otolith biomineralization, was shown to be weakly present in the EDTA-soluble organic fractions. Such a structuring organic fraction would be relatively more present in the D-zones such that these zones would be less affected by EDTA etching, providing an explanation to the inversion observed before and after acid etching in terms of relative proportion of the organic and mineral compounds.

The agreement between the Raman characterization of the responses of CH and Mutvei's staining in L- and D-zones may also be interpreted as an evidence that CH signatures are associated with otolith organic compounds such as polysaccharides, glycosaminoglycans and proteoglycans. An additional evidence supports this assumption.

316 Mutvei's solution was shown to underline water-soluble macromolecules (polysaccharides)
317 previously reported to play a key role in biomineralization and in particular in the nucleation
318 of otolith [26]. This is in accordance with the strong CH-response observed on Raman spectra
319 on the primordium.
320

321 ## Conclusion

322 A lot of effort have been devoted to the analysis of the chemical composition of the otolith
323 [38] at scales from one up to hundreds of micrometers depending on the chemical signatures
324 of interest (e.g., elemental composition, isotopic ratios) and on the considered analytical
325 method (e.g., WDS, LA-ICPMS, IRMS) [38-40]. Such chemical analysis provide data that are
326 required for specific fisheries issues (e.g. reconstructing individual life traits, analysing
327 population structure etc.) . However they do not supply information on the relative organic
328 and mineral fractions of the otolith which knowledge plays a key role in the understanding of
329 the underlying biomineralization processes.

330 Because Raman micro-spectrometry (unlike Fourier transformed infrared
331 spectroscopy) has potential for non destructive and micro-scale diagnostics, this study was
332 designed to quantify and characterize organic and mineral fractions in otoliths structures. The
333 main contributions, exemplified here by the determination of the relative spatial variations of
334 the AR and CH fractions are three-fold: 1) the simultaneous analysis of the organic and
335 mineral fractions of the otolith; 2) a subscale analysis (1µm) corresponding to daily if not
336 subdaily timescales on otolith sections; 3) a quantitative characterization through the
337 magnitude of specific peaks observed in the Raman spectra. The Raman-based analysis shows
338 that fine scale otolith structures depict variations both in absolute and relative concentrations
339 of mineral and organic compounds. This finding challenges the current perception of L- and
340 D- zones in terms of mineral and organic compounds. In relation to the daily eurhythmics

observed in L- and D-zone deposition, concentrations in endolymph organic precursors and total CO_2 depict circadian cycles [41-43], in antiphasic ryhtm [4, 44]. Raman spectra reflected cyclic variations according to alternation of L- and D-zones but with synchronous variations between CH and AR. This could be explained by the fact that the CH-signature does not involve all the organic compounds present in the endolymph (proteins, collagens, proteoglycans, inhibitor factor). *In situ* Raman analysis of the endolymph along a daily cycle might validate this assumption.

Future work will be aimed at refining our analysis of the Raman spectra. In the present study, we mainly focused on two specific Raman signatures, the responses of the aragonitic fractions observed at 1085 cm^{-1} and the responses of organic compounds involving CH-groups observed at 2950 cm^{-1}. Raman spectra convey much more information and future works will aim to better relate Raman signatures to known specific organic compounds (e.g., isolated proteins, sugars, proteoglycans) using complementary tools (electrophoresis or immuno-histochemical analysis).

References

1. Panfili J, de Pontual H, Troadec H, Wright PJ (2002) Manual of fish Sclerochronology. Ifremer-IRD Coeditions, Brest, France.
2. Pannela G (1971) Science 173: 1124-1127.
3. Campana SE (2005) Mar Freshwat Res 56: 485-495.
4. Allemand D, Mayer-Gostan N, de Pontual H, Boeuf G, Payan P (2007) Fish otolith calcification in relation to endolymph chemistry. In: Baeuerlein E (ed.) Handbook of Biomineralization: Biological aspects and structure formation.
5. Borelli G, Mayer-Gostan N, Merle PL, De Pontual H, Boeuf G, Allemand D, Payan P (2003) Calcif Tissue Int 72: 717-725.

366 6. Murayama E, Okuno A, Ohira T, Takagi Y, Nagasawa H (2000) Comp Biochem
367 Physiol 126B: 511-520.
368 7. Murayama E, Takagi Y, Ohira T, Davis JG, Greene MI, Nagasawa H (2002) Eur J
369 Biochem 269: 688-696.
370 8. Söllner C, Burghammer M, Busch-Nentwich E, Berger J, Schwarz H, Riekel C,
371 Nicolson T (2003) Science 302: 282-286.
372 9. Campana SE (1999) Mar Ecol Progr Ser 188: 263-297.
373 10. McCreadie BR, Morris MD, Chen T-C, Rao DS, Finney WF, Widjaja E, Goldstein SA
374 (2006) Bone 39: 1190-1195.
375 11. Payan P, De Pontual H, Edeyer A, Borelli G, Boeuf G, Mayer-Gostan N (2004) Can J
376 Fish Aquat Sci 61: 1247-1255.
377 12. Gauldie RW, Sharma SK, Volk E (1997) Comp Biochem Physiol 118A: 753-757.
378 13. Melancon S, Fryer BJ, Ludsin SA, Gagnon JE, Yang ZP (2005) Can J Fish Aquat Sci
379 62: 2609-2619.
380 14. Tomás J, Geffen AJ (2003) J Fish Biol 63: 1383-1401.
381 15. Tzeng WN, Chang CW, Wang CH, Shiao JC, Iizuka Y, Yang YJ, You CF, Ložys L
382 (2007) Mar Ecol Progr Ser 348: 285-295.
383 16. Kaczorowska B, Hacura A, Kupka T, Wrzalik R, Talik E, Pasterny G, Matuszewska A
384 (2003) Anal Bioanal Chem 377: 1032-1037.
385 17. Perrin C, Smith DC (2007) C R Palevol 6: 253-260.
386 18. Hedegaard C, Bardeau J-F, Chateigner D (2006) J Mollus Stud 72: 157-162.
387 19. Zhang F, Cai W, Sun Z, Zhang J (2008) Anal Bioanal Chem 390: 777-782.
388 20. Schöne BR, Dunca E, Fiebig J, Pfeiffer M (2005) Palaeogeogr, Palaeoclimatol,
389 Palaeoecol 228: 149-166.
390 21. Urmos J, Sharma SK, Mackenzie FT (1991) Am Miner 76: 641-646.

391 22. Careche M, Herrero AM, Rodriguez-Casado A, Del Mazo ML, Carmona P (1999) J
392 Agr Food Chem 47: 952-959.
393 23. Ikoma T, Kobayashi H, Tanaka J, Walsh D, Mann S (2003) Int J Biol Macromol 32:
394 199-204.
395 24. Piot O, Autran J-C, Manfait M (2000) J Cereal Sci 32: 57-71.
396 25. Morales-Nin B (1987) Ultrastructure of the organic and inorganic constituents of the
397 otoliths of the sea bass. In: Summerfeld RC, Hall GE (eds) The Age and Growth of
398 Fish. The Iowa State University Press, Ames, Iowa.
399 26. Pisam M, Jammet C, Laurent D (2002) Cell Tissue Res 310: 163-168.
400 27. Dunkelberger DG, Dean JM, Watabe N (1980) J Morphol 163: 367-377.
401 28. Fay RR (1984) Science 225: 951-954.
402 29. Platt C, Popper AN (1981) Fine structure and function of the ear. In: Tavolga WN,
403 Popper AN, Fay RR (eds) Hearing and Communication in Fishes. Springer-Verlag,
404 New York.
405 30. Pisam M, Payan P, LeMoal C, Edeyer A, Boeuf G, Mayer-Gostan N (1998) Cell
406 Tissue Res 294: 261-270.
407 31. Alvarez P, Cotano U (2005) Fish Res 76: 379-391.
408 32. Secor DH, Dean JM, Laban EH (1992) Otolith removal and preparation for
409 microstructural examination. In: Stevenson DK, Campana DK (eds) Otolith
410 microstructure examination and analysis. Can Spec Publ Fish Aquat Sci.
411 33. Marxen JC, Hammer M, Gehrke T, Becker W (1998) Biol Bull 194: 231-240.
412 34. Alldredge AL, Passow U, Logan BE (1993) Deep Sea Res I 40: 1131-1140.
413 35. Wright PJ (1991) J Fish Biol 38: 625-627.
414 36. Borelli G, Mayer-Gostan N, De Pontual H, Boeuf G, Payan P (2001) Calcif Tissue Int
415 69: 356-364.

37. Dauphin Y, Dufour E (2003) Comp Biochem Physiol 134A: 551-561.

38. de Pontual H, Geffen AJ (2002) Otolith microchemistry. In: Panfili J, de Pontual H, Troadec H, Wright PJ (eds) Manual of Fish Sclerochronology. Coedition Ifremer-IRD, Brest, France.

39. de Pontual H, Lagardère F, Amara R, Bohn M, Ogor A (2003) J Sea Res 50: 199-210.

40. Tomás J, Geffen AJ, Millner RS, Pineiro CG, Tserpes G (2006) Mar Biol 148: 1399-1413.

41. Borelli G, Guibbolini ME, Mayer-Gostan N, Priouzeau F, de Pontual H, Allemand D, Puverel S, Tambutte E, Payan P (2003) J Exp Biol 206: 2685-2692.

42. Edeyer A, de Pontual H, Payan P, Troadec H, Sévère A, Mayer-Gostan N (2000) Mar Ecol Progr Ser 192: 287-294.

43. Mugiya Y (1987) Fish Bull 85: 395-401.

44. Payan P, de Pontual H, Boeuf G, Mayer-Gostan N (2004) C R Palevol 3: 535-547.

45. Briget Mary M, Ramakrishnan V (2005) Spectrochimica Acta Part A 62: 164-170.

Table 1: Details on otoliths samples investigated by Raman micro-spectrometry: fish origin and size (cm), thickness (µm) and type of otolith section (transversal or sagittal), preparation method, analyzed area and characteristics of the analysis (T: transect, M: Mapping, D: Distance between two analysed points).

Name	Origin	Size (cm)	Thickness (µm)	Section	Preparation method	Area	Analysis	
S1	Rearing	25	150	Transversal	Standard	Core	T: 20µm	S: 6µm
S2	Wild	33	394	Transversal			T: 40µm	S: 2.5µm
S3	Wild	20	325	Transversal			T: 40µm	S: 2.5µm
				Transversal			2D-M: 30µm x 40µm	S X: 2.5µm
								S Y: 3µm
S4	Rearing	4.3 mm		Sagittal			T: 15µm	7, 12, 14 µm
S5	Wild	21	100	Sagittal		L- and D-zones	T: 44µm	S: 0.7µm
S6	Wild	34	299	Sagittal			T: 36µm	S: 0.8µm
S7	Wild	20	375	Transversal	Acid etching		T: 12µm	S: 0.7µm
S8	Wild	30	132	Transversal	Mutvei's staining		T: 5µm	S: 0.2µm

436 **Table 2**: Wavenumbers and assignments of the Raman bands observed in the core area:
437 comparisons between results reported by Zhang *et al.* (2008) on small yellow croaker and
438 sample S1 from our study. In the table, NS is indicated a non significant intensity on Raman
439 spectra.

Wavenumbers (cm^{-1}) Zhang (2008)	**Wavenumbers (cm^{-1}) Samples S1-S4**	**Band attribution [19, 22-24, 45]**
	641	$(SO_4)^{2-}$ asym bend
765	755	Trp, Amide IV, V
830	824	ν- ring, Tyr, Ac Asp
853	853	δ(CCH) ring, ν(C-C), Tyr, Ac asp
880	878	δ(CCH) ring, Trp, Val, Hyp
940	937	Nonaromatic ν(C-C), Lys, Val, Leu
1003	NS	Phe
1031	NS	Phe
	1085	Aragonite
	1110	ν CN
	1185	Tyr
	1200-1272	amide III
1272	NS	amide III
1297	1297	δ(C=H), phospholipids
1443	1444	CH_2, CH, CH_3 bending
1461	1460	Aragonite
1555	NS	Trp
1574	1574	Aragonite
	1610	Trp, Phe, Tyr ν-ring
1660		Amide I
2852	2851	$\nu(CH_2)_{sym}$ lipids
2882	2876	$\nu(CH_2)_{asym}$ lipids, $\nu(CH_2)_{sym}$ proteins
2942	2941	$\nu(CH_3)_{sym}$ proteins and lipids, $\nu(CH_2)_{asym}$ proteins
	3067	CH stretch

440

441 **Figure legends**

442 **Figure 1:** Otolith structures at macro and microsocopic scales. a) Transverse section of a hake
443 otolith observed under reflected light showing opaque (O) and translucent (T) zones. Opaque
444 zones appear dark in transmitted light and bright in reflected light, and vice versa for
445 translucent zones. The core (C) corresponds to the area surrounding the primordium which is
446 the initial structure of otolith. Scale bar: 1 mm. b) Thin transverse section of a hake otolith
447 under transmitted light microscopy. Primary increments composed of L- and D-zones are
448 clearly visible. Scale bar: 10 µm

449 **Figure 2:** Raman spectrum acquired on sample S5: the spectrum is dominated by the response
450 of Aragonite (in dotted line) in the frequency range 100-4000 cm^{-1} but also reveals (B) the
451 presence of organic matrix (in black solid line) with main response on CH-peak in the
452 frequency range 1000-4000 cm^{-1}.

453 **Figure 3:** Raman spectra of Mutvei's solution (in dark) and on S8 stained with Mutvei's
454 solution (in grey): the main signature of the staining agent between 500 and 2000 cm^{-1} (514.5
455 nm wavelength radiation, laser power of 20 mW and acquisition time of 20 s, 20 times). The
456 two grey areas underline aragonite signatures (100-300 cm^{-1}) and Mutvei's solution signatures
457 (1200-1700 cm^{-1}) considered for the analyses.

458 **Figure 4:** (A) Typical view of S1 thin section obtained by light microscopy. The ventral (V)
459 and dorsal (D) area are shown as well as the source point positions (adjacent points are
460 separated by 6 µm) where spectra were collected (scale bar = 5 µm); (B) Raman spectra
461 acquired along the considered dorso-ventral transect in the 100-4000 cm^{-1} region. For clarity,
462 the spectra are only shifted (and not background corrected).

463 **Figure 5:** Normalized integrated intensity of OM/AR calculated for S1 to S4 in the
464 primordium area. (A) CH/AR (in dark) and OH/AR (in grey) as a function of the distance
465 from the primordium for the sample S1. (B) Evolution of CH/AR signature (CH/AR was

normalised by CH/AR from the primordium) as a function of the distance from the primordium for samples S1 to S4.

Figure 6: (A) View of S3 thin section under light microscopy. The rectangle (30 µm x 40 µm) centred on primordium, represents the 2D Raman mapping area: step increments were fixed to 3 µm and 2.5 µm in the X and Y directions respectively (scale bar = 10 µm); (B) XY micro Raman mapping of the normalized integrated intensity of CH/AR (D: dorsal, V: ventral, S: sulcus AS: antisulcus). Coordinates were focused on primordium (µm).

Figure 7: (A) Typical view of S5 thin section obtained by light microscopy; (B) Raman spectra in the 2500-4000 cm^{-1} region of one L-zone (dark spectrum) and one D-zone (grey spectrum) on S5 (scale bar = 5 µm).

Figure 8: (A) Typical view of S5 thin section under light microscopy. Markers delimit the successive L- and D-zones (scale bar = 5 µm); (B) Integrated Raman intensities of AR (dark line) and CH (grey line) along the line direction. (C) Evolution of CH/AR with D-zones depicted as grey areas.

Figure 9: (A) Typical view of S7 thin section of otolith obtained under light microscopy before acid etching. Markers delimit the successive L- and D-zones (scale bar = 5µm); (B) Evolution of CH/AR before (grey line) and after (dark line) acid etching with D-zones marked by grey areas.

Figure 10: Integrated surfaces of Mutvei's and AR signatures and Mutvei's/AR from Raman spectra after Mutvei's staining on sample S8. Analyses were made on transect covering 3 L-zones and 2 D-zones. (A) Evolution of the AR (dark line) and Mutvei's solution (grey line) responses on otolith. (B) Evolution of the ratio between Mutvei's and AR signatures as a function of the position along the transect.

Figure 1:

(A)

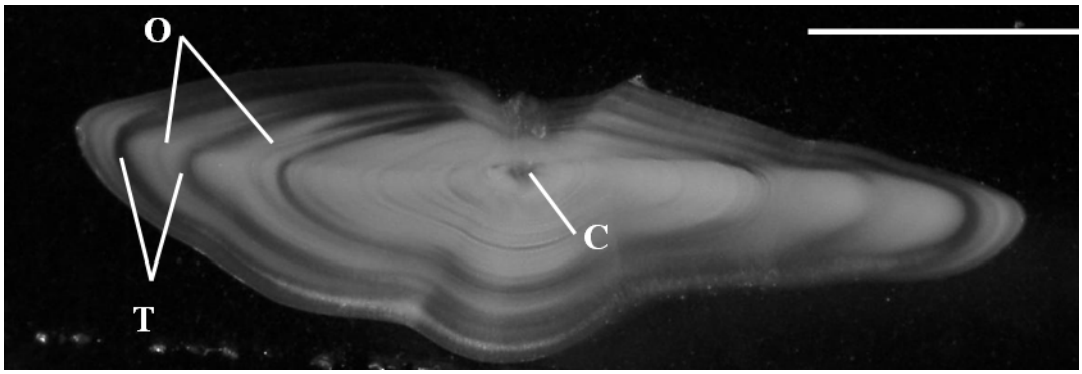

(B)

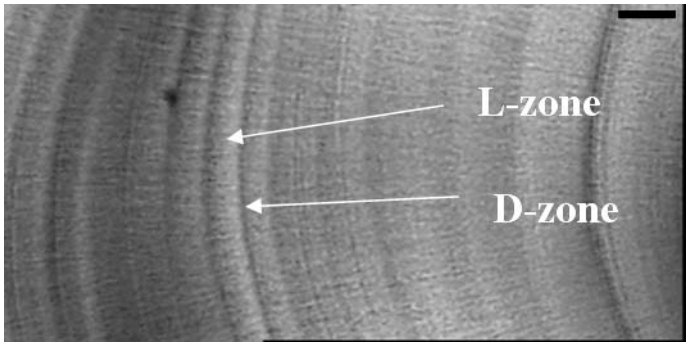

494 **Figure 2:**

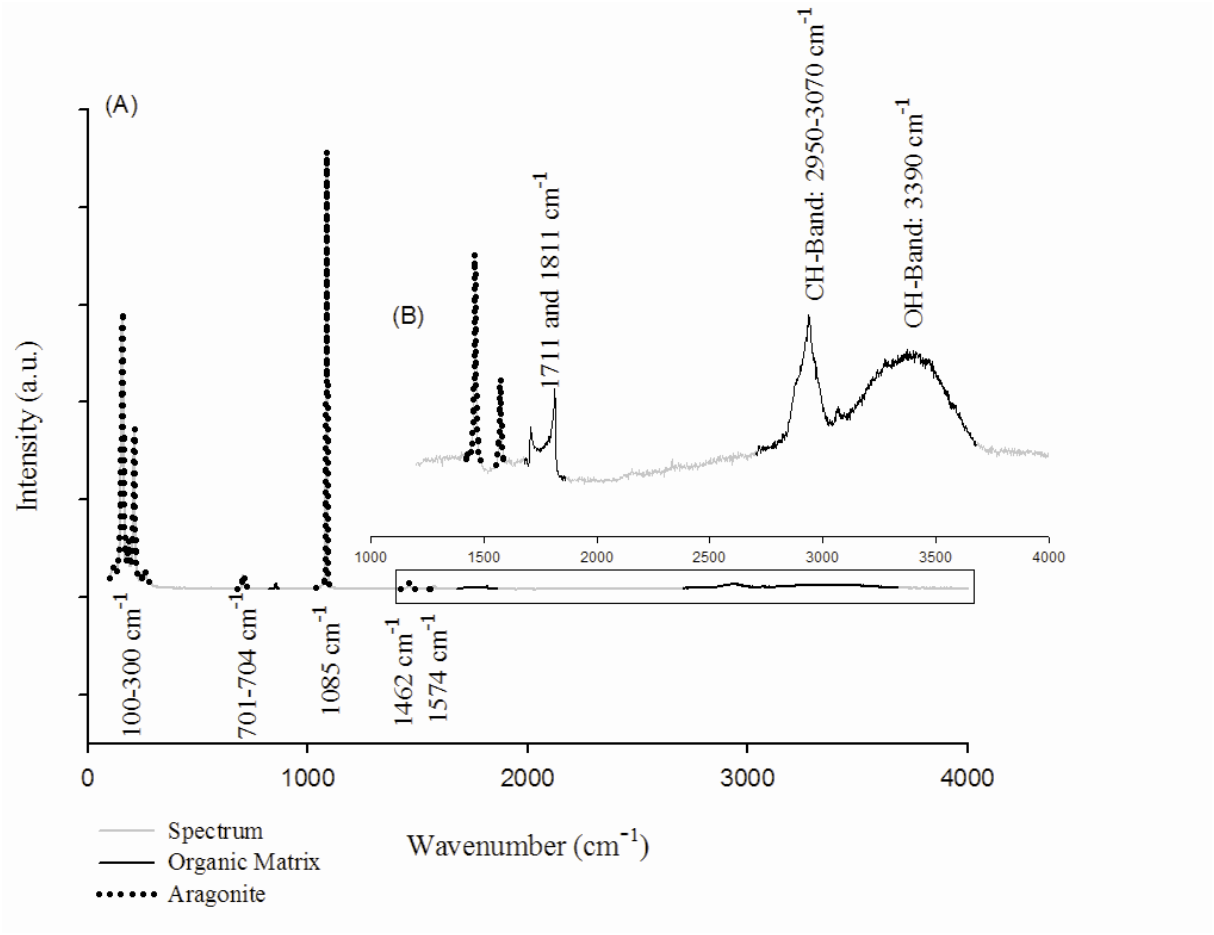

495

496 **Figure 3:**

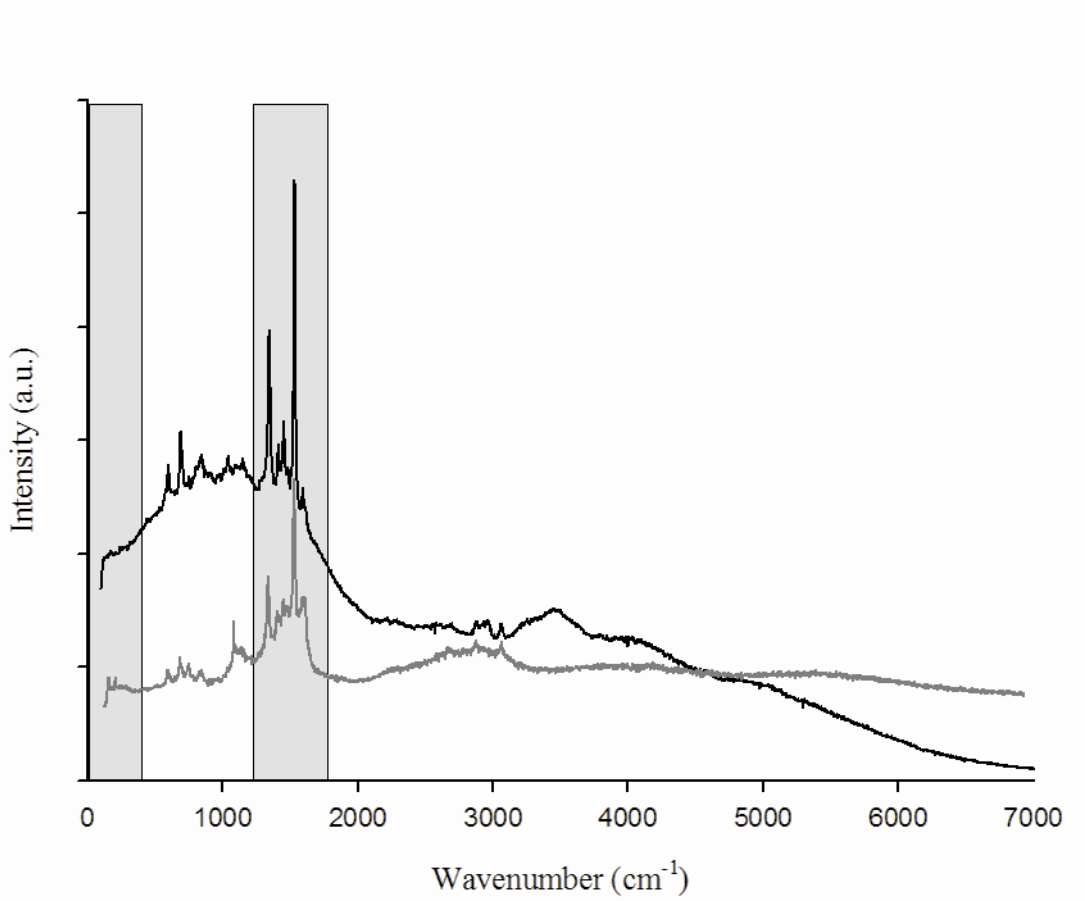

497

Figure 4:

(A)

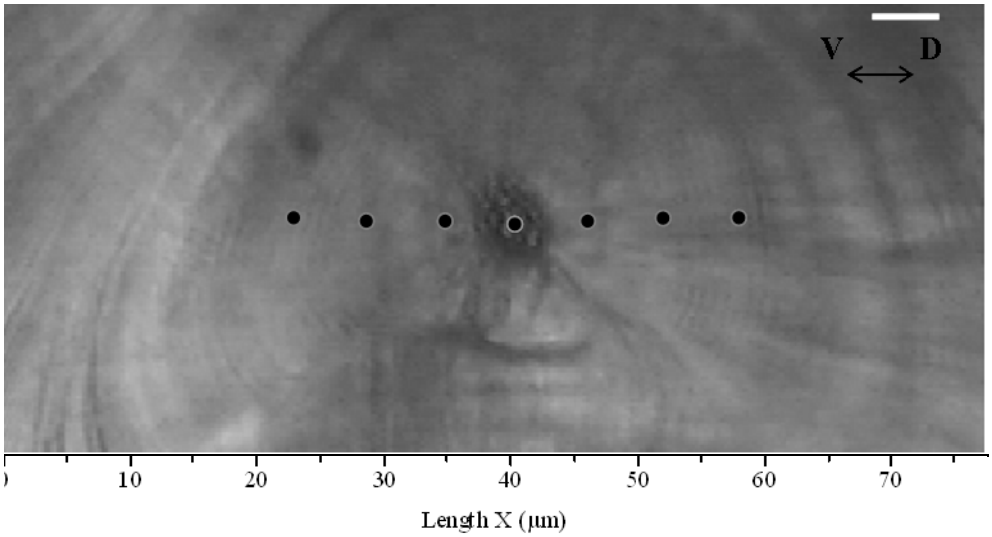
V
D
10
20
30
40
50
60
70
Length X (µm)

(B)

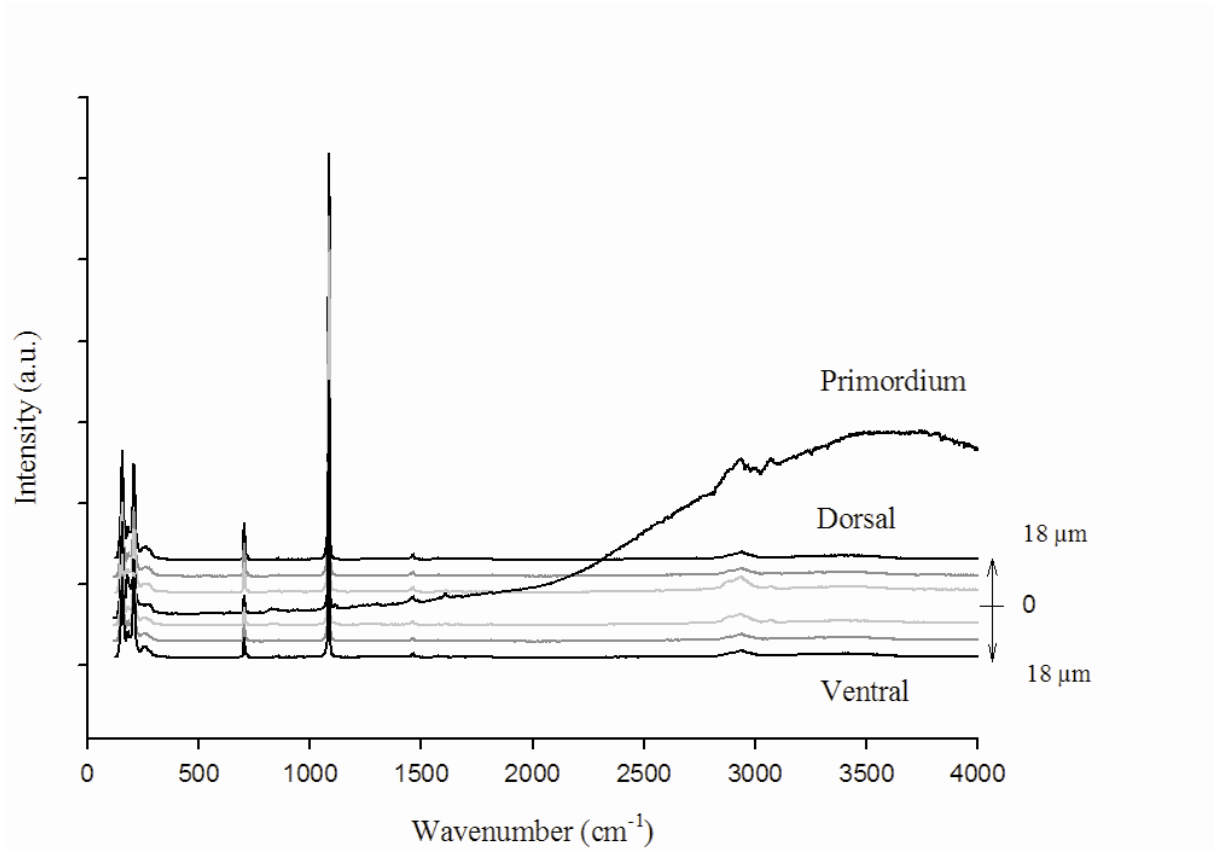
Intensity (a.u.)
Primordium
Dorsal
18 µm
0
18 µm
Ventral
0
500
1000
1500
2000
2500
3000
3500
4000
Wavenumber (cm-1)

Figure 5:

(A)

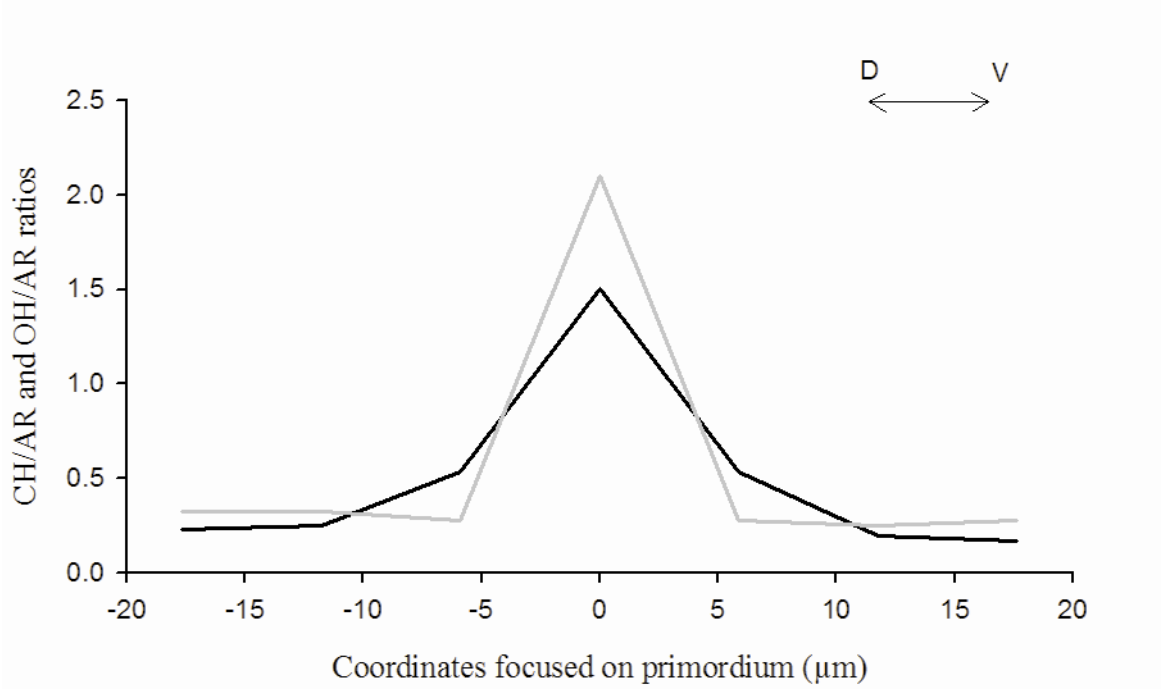
D
V
2.5
2.0
1.5
1.0
0.5
0.0
CH/AR and OH/AR ratios
-20
-15
-10
-5
0
5
10
15
20
Coordinates focused on primordium (µm)

(B)

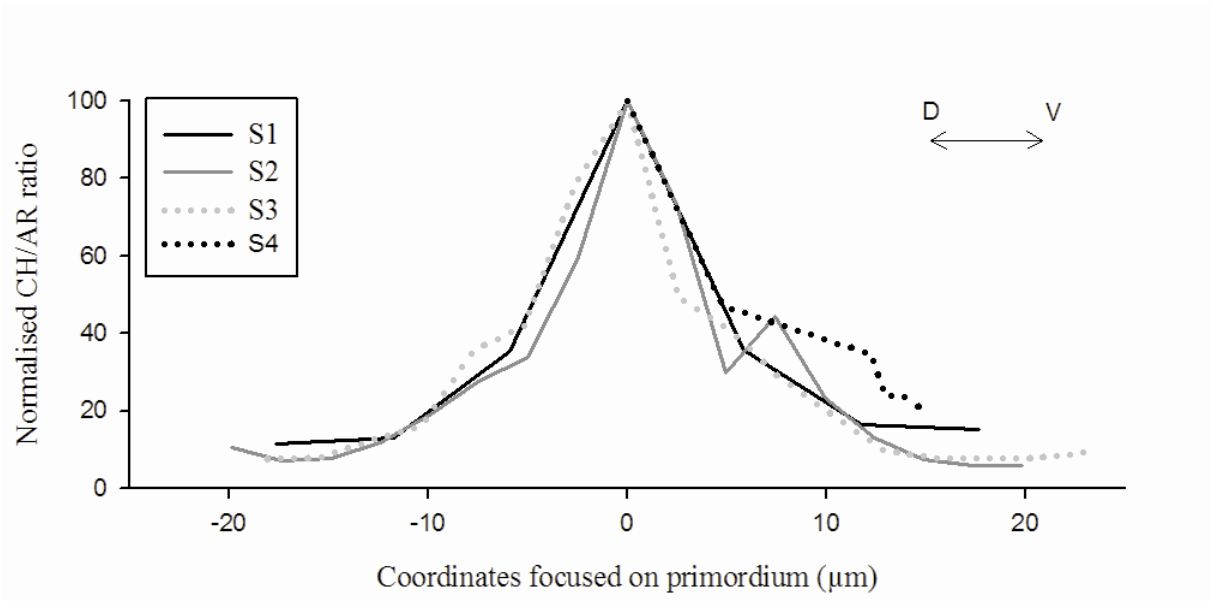
S1
S2
S3
S4
D
V
100
80
60
40
20
0
Normalised CH/AR ratio
-20
-10
0
10
20
Coordinates focused on primordium (µm)

Figure 6:

(A)

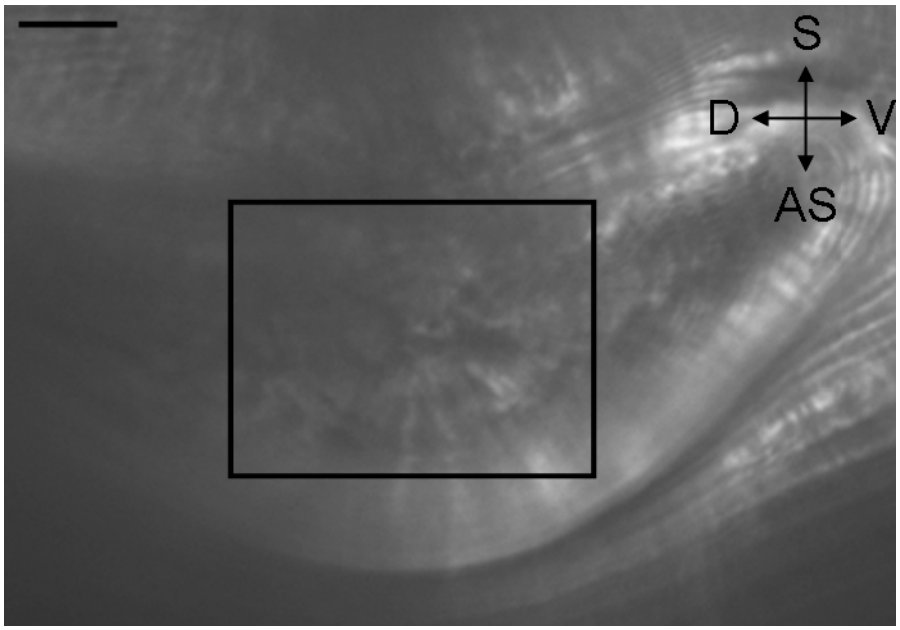

(B)

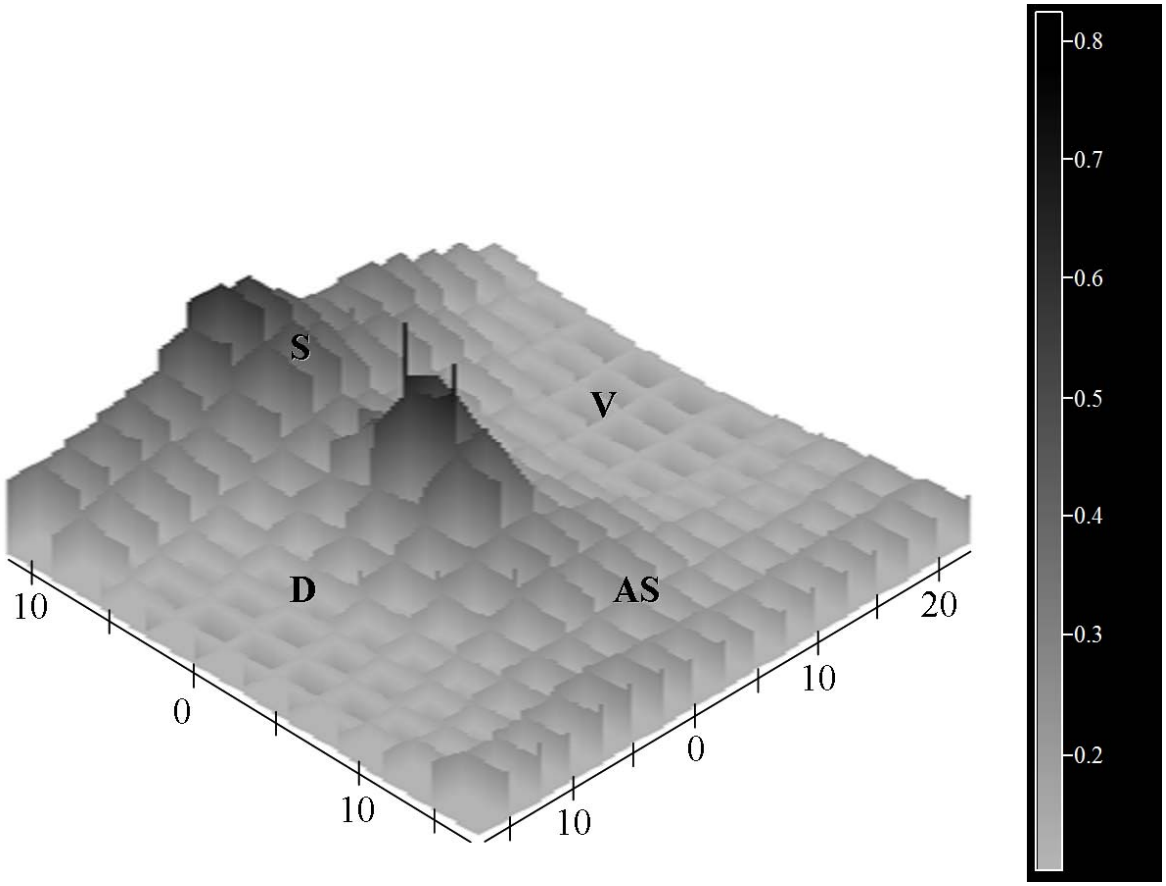

513 Figure 7:

514 (A)

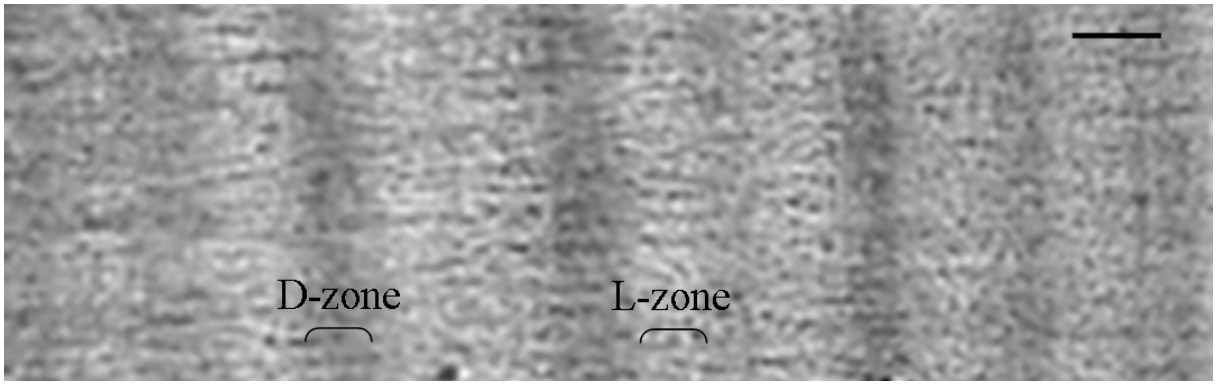

515

516 (B)

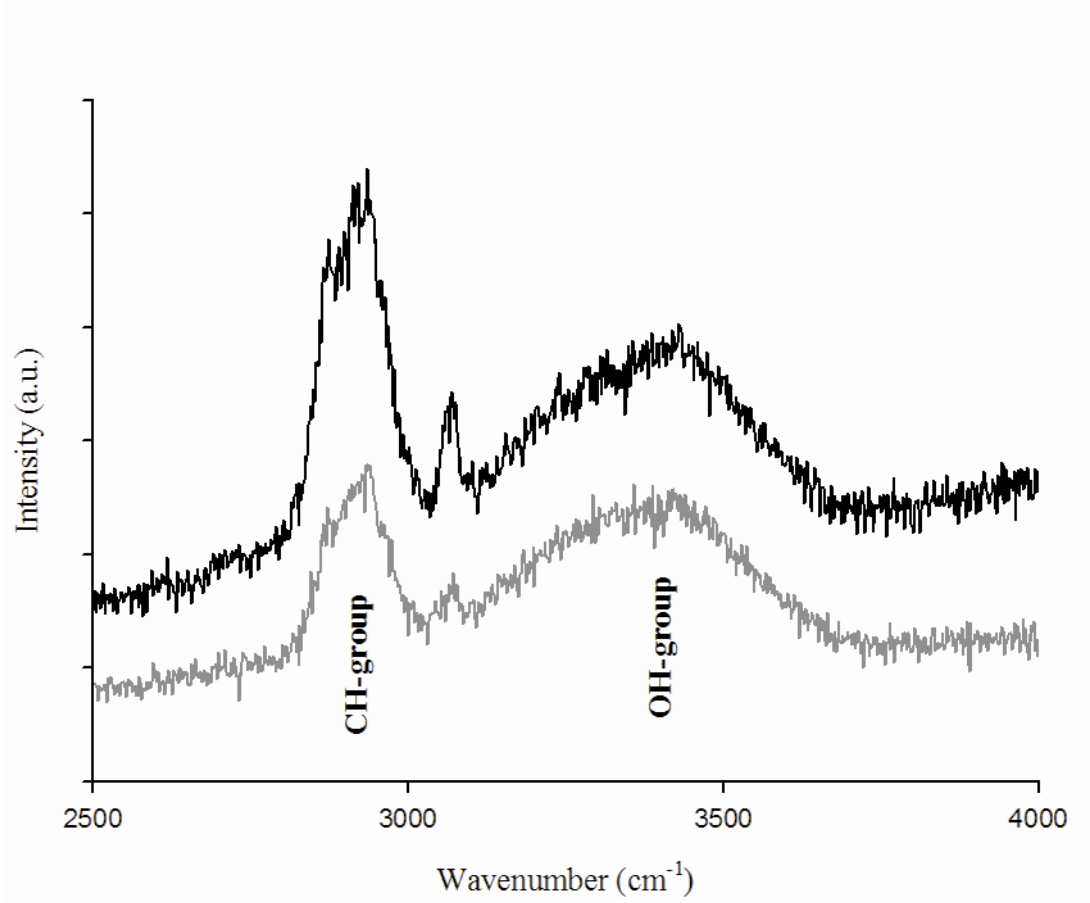

517

Figure 8:

(A)

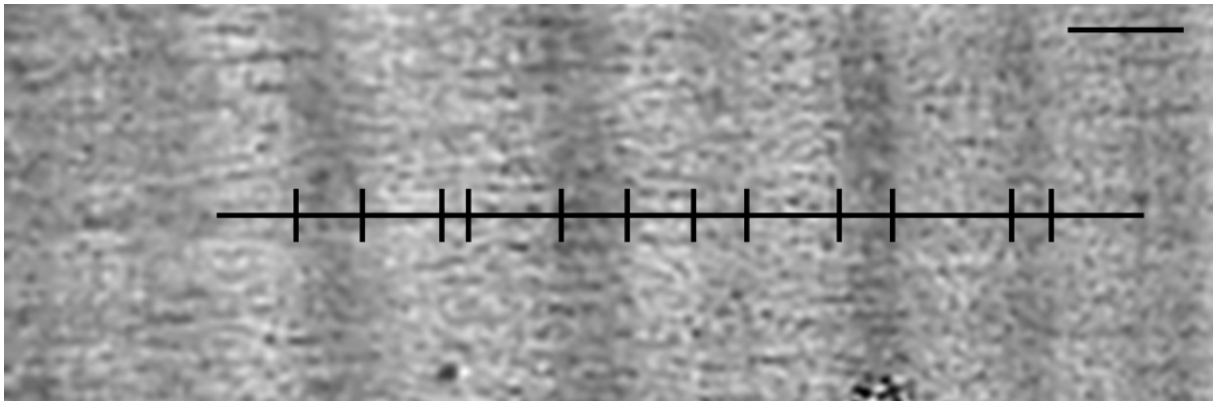

(B)

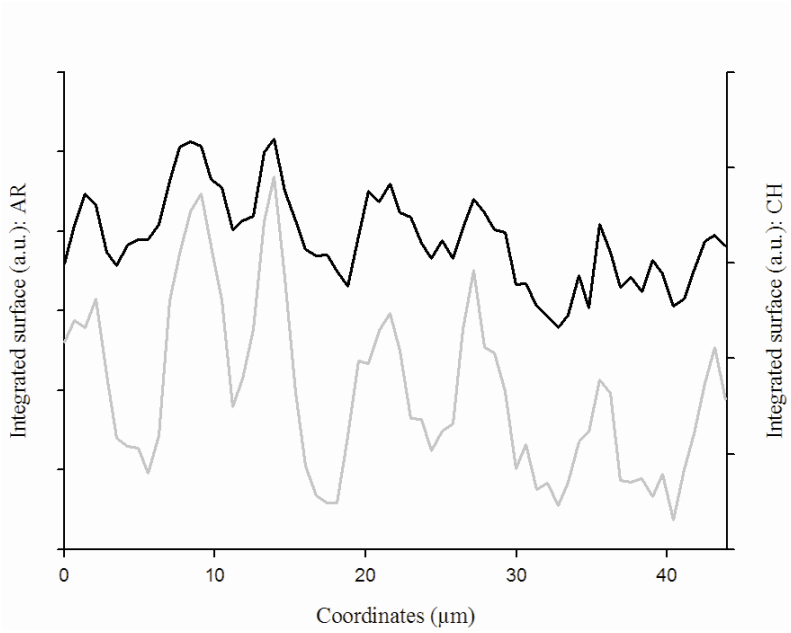
Integrated surface (a.u.): AR
Integrated surface (a.u.): CH
0
10
20
30
40
Coordinates (µm)

(C)

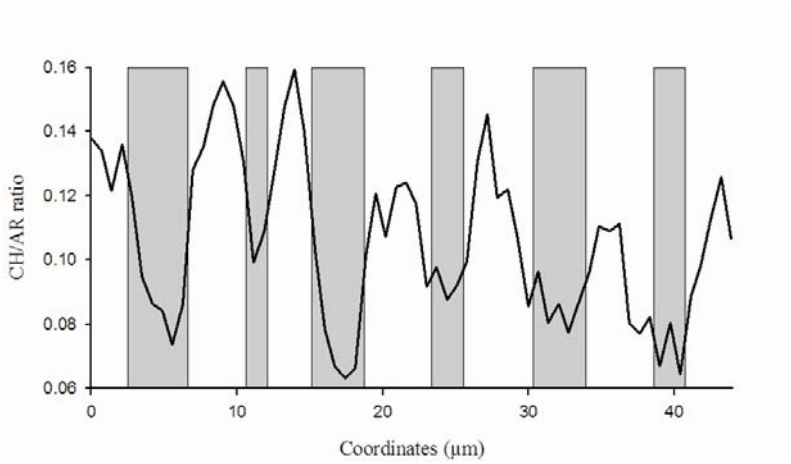
CH/AR ratio
0.16
0.14
0.12
0.10
0.08
0.06
0
10
20
30
40
Coordinates (µm)

Figure 9:

(A)

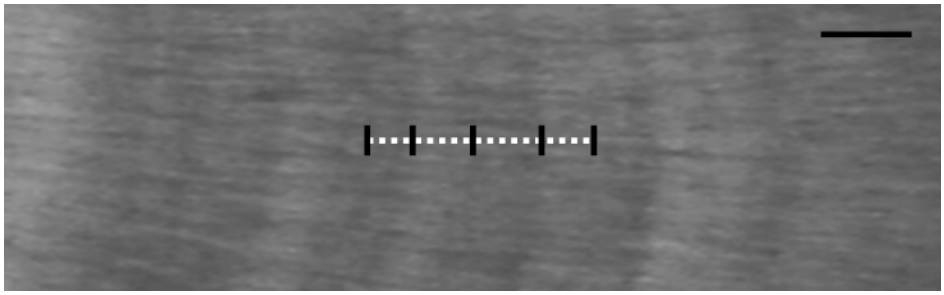

(B)

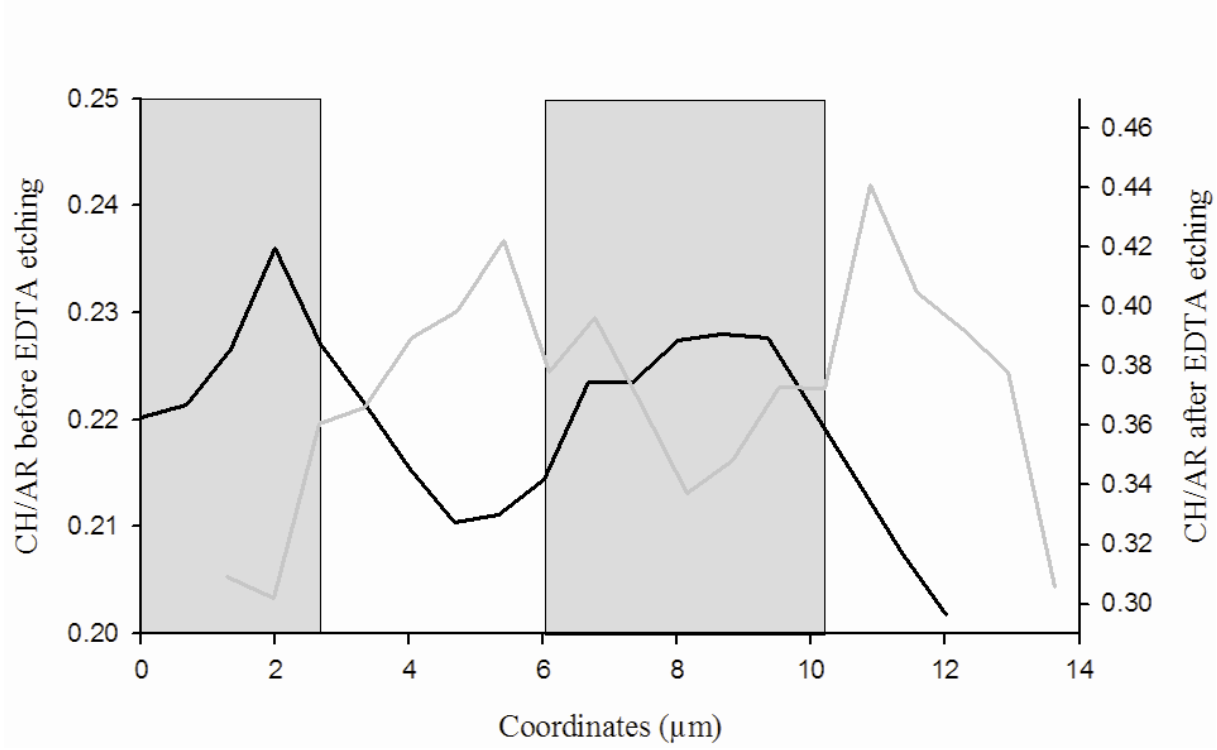
CH/AR before EDTA etching
CH/AR after EDTA etching
Coordinates (µm)
0.25
0.24
0.23
0.22
0.21
0.20
0.46
0.44
0.42
0.40
0.38
0.36
0.34
0.32
0.30
0
2
4
6
8
10
12
14

Figure 10:

(A)

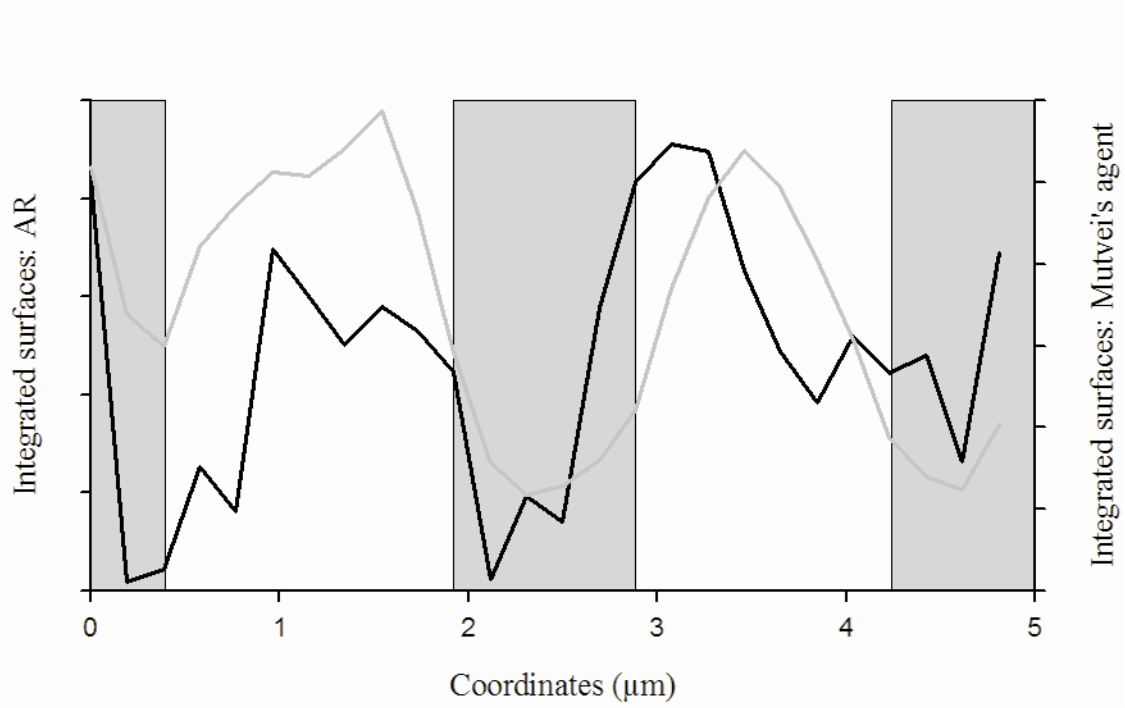
Integrated surfaces: AR
Integrated surfaces: Mutvei's agent
0
1
2
3
4
5
Coordinates (µm)

(B)

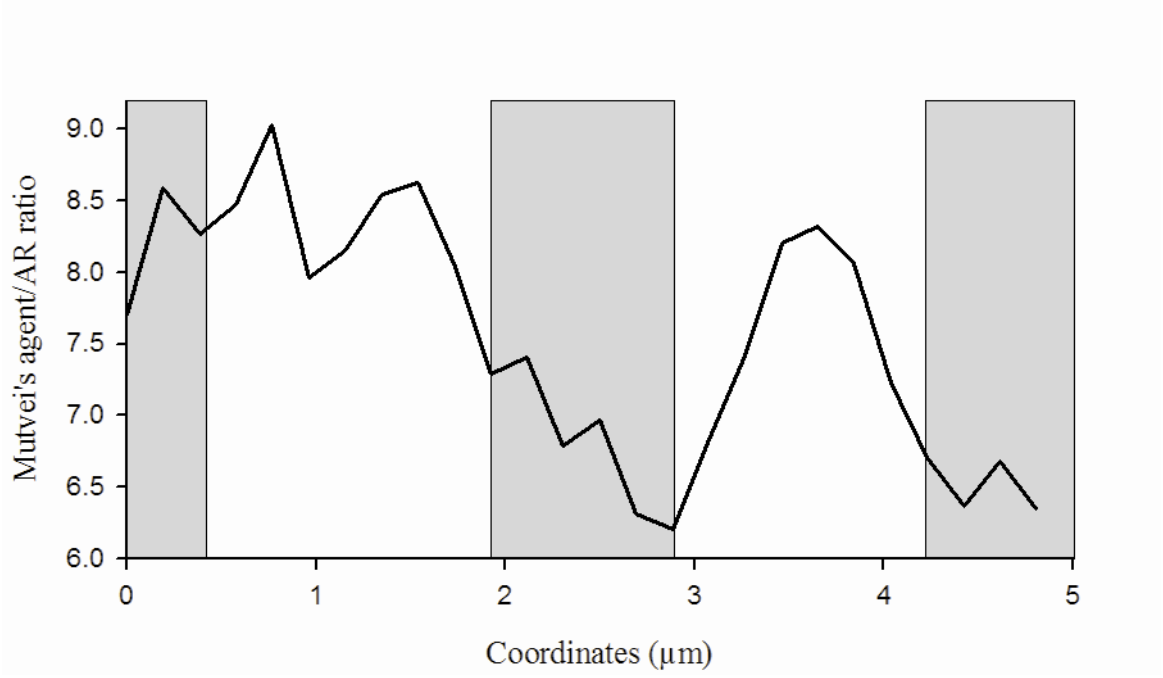
Mutvei's agent/AR ratio
9.0
8.5
8.0
7.5
7.0
6.5
6.0
0
1
2
3
4
5
Coordinates (µm)